Chemical Science

ROYAL SOCIETY OF CHEMISTRY

EDGE ARTICLE

Cite this: *Chem. Sci.*, 2024, **15**, 8242

All publication charges for this article have been paid for by the Royal Society of Chemistry

Received 13th July 2023
Accepted 4th February 2024

DOI: 10.1039/d3sc03606e

rsc.li/chemical-science

Cluster dynamics of heterometallic trinuclear clusters during ligand substitution, redox chemistry, and group transfer processes†

Cristin E. Juda, Rex C. Handford, Amymarie K. Bartholomew, Tamara M. Powers, Nina X. Gu, Elisabeth Meyer, Nikolaj Roth, Yu-sheng Chen, Shao-Liang Zheng and Theodore A. Betley *

Stepwise metalation of the hexadentate ligand $^{tbs}LH_6$ ($^{tbs}LH_6$ = 1,3,5-$C_6H_9(NHC_6H_4$-*o*-$NHSiMe_2{}^tBu)_3$) affords bimetallic trinuclear clusters (^{tbs}L)Fe_2Zn(thf) and (^{tbs}L)Fe_2Zn(py). Reactivity studies were pursued to understand metal atom lability as the clusters undergo ligand substitution, redox chemistry, and group transfer processes. Chloride addition to (^{tbs}L)Fe_2Zn(thf) resulted in a mixture of species including both all-zinc and all-iron products. Addition of ArN_3 (Ar = Ph, 3,5-$(CF_3)_2C_6H_3$) to (^{tbs}L)Fe_2Zn(py) yielded a mixture of two trinuclear products: (^{tbs}L)$Fe_3(\mu^3$-NAr) and (^{tbs}L)$Fe_2Zn(\mu^3$-NAr)(py). The two imido species were separated *via* crystallization, and outer sphere reduction of (^{tbs}L)$Fe_2Zn(\mu^3$-NAr)(py) resulted in the formation of a single product, [2,2,2-crypt(K)][(^{tbs}L)$Fe_2Zn(\mu^3$-NAr)]. These results provide insight into the relationship between heterometallic cluster structure and substitutional lability and could help inform both future catalyst design and our understanding of metal atom lability in bioinorganic systems.

1 Introduction

Metalloenzyme cofactors (*e.g.*, FeMoco in nitrogenase,[1–4] oxygen evolving complex (OEC) in photosystem II[5–9]) and heterogeneous catalysts (*e.g.*, Haber–Bosch,[10,11] Fischer–Tropsch[12]) are known to utilize polynuclear reaction sites to afford multielectron redox chemistry. However, full mechanistic understanding of these catalytic reactions remains elusive primarily due to the challenges associated with reaction monitoring.[2,3,12,13] Consequently, synthetic polynuclear clusters, readily studied using a variety of spectroscopic techniques, have been developed as models for polynuclear active sites of biological[14–22] and abiological[23] catalysts. The breadth of spectroscopic methods for monitoring the reactivity of synthetic clusters allows one to probe cluster dynamics in a variety of chemical reactions. Specifically, we are interested in probing metal atom lability and changes in coordination geometry during reaction processes. The extent to which these processes occur can provide insight into how cluster integrity changes during chemical transformations.

We are particularly interested in investigating metal atom lability in synthetic heterometallic clusters given the prevalence of metalloenzyme heterometallic cofactors (*e.g.*, nitrogenase cofactors,[1–4,24–26] carbon monoxide dehydrogenase,[27–30] OEC,[5–9,31,32] and the Mn/Fe cofactor in ribonucleotide reductase,[33–35] see Fig. 1) as well as their conformational lability in during reactivity (*e.g.*, nitrogenase, OEC).[24,26,29–32] Given these motivations we sought to use a mixed-metal system to uncover fundamental principles of how cluster binding geometry and reactivity relate to metal atom lability within synthetic analogues.

Our lab has previously employed a hexadentate ligand, 1,3,5-C_6H_9-$(NHC_6H_4$-*o*-$NHSi^tBuMe_2)_3$ ($^{tbs}LH_6$), to yield both homo-[21,36–38] and hetero-trinuclear[39] clusters, including reactive,

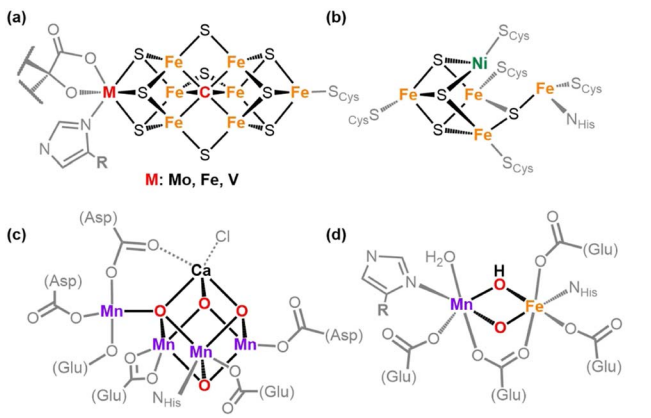

Fig. 1 Example heterometallic cofactors in nature: (a) nitrogenase, (b) carbon monoxide dehydrogenase, (c) oxygen evolving complex, and (d) MnFe ribonucleotide reductase.

Department of Chemistry and Chemical Biology, Harvard University, Cambridge, MA 02139, USA. E-mail: betley@chemistry.harvard.edu

† Electronic supplementary information (ESI) available. CCDC 1993457–1993469. For ESI and crystallographic data in CIF or other electronic format see DOI: https://doi.org/10.1039/d3sc03606e

high spin (^{tbs}L)Fe$_3$(thf) (**1**) and (^{tbs}L)Fe$_3$(py) (**2**). Treatment of **1** with small molecule substrates results in multi-electron bond activation processes.[36] Previous work by our lab has also demonstrated that reactive, high-spin clusters can undergo metal atom metathesis.[40] Therefore, to test the metal atom lability of our clusters during reactions, we sought to explore reaction chemistry on a heterometallic trinuclear cluster. In this work, we describe the synthesis of [Fe$_2$Zn] clusters and assess their substitutional integrity as they undergo substrate binding, oxidative group transfer, and outer sphere redox chemistry. In both substrate binding and group transfer chemistry, we observe redistribution of metals, whereas in the presence of a μ^3-imido cap on the clusters, the cluster core maintains its integrity during redox processes. The results presented herein illustrate that for open-shell clusters, metal atom exchange can be facile even when starting with substitutionally homogeneous materials. This point is especially important given the formation of heterometallic enzymatic cofactors that do not necessarily feature electronically differentiated binding sites. Thus, formation of heterometallic species might form under mild conditions.

2 Results and discussion

2.1. Synthesis of diiron zinc trinuclear clusters

A transmetalation strategy was employed to synthesize the targeted [Fe$_2$Zn] clusters. The Fe/Zn combination allows for the facile determination of metal atom composition *via* X-ray fluorescence (XRF) spectroscopy, as the Kα lines differ significantly in energy. Additionally, the large difference in atomic scattering factors for Fe and Zn potentially enables their discrimination through single-crystal X-ray diffraction (SC-XRD) analysis. In the absence of coordinating solvent, metalation of ^{tbs}LH$_6$ with Fe$_2$(N(SiMe$_3$)$_2$)$_4$ forms (^{tbs}LH$_2$)Fe$_2$ (**3**; Scheme 1). Deprotonation of **3** with Na(N(SiMe$_3$)$_2$) (2 equiv.) in thawing THF yielded [Na(thf)][(^{tbs}L)Fe$_2$Na(thf)] (**4**). Addition of **4** to a frozen suspension of ZnCl$_2$ in THF afforded (^{tbs}L)Fe$_2$Zn(thf) (**5**), which was crystallized from a mixture of hexane and benzene at −33 °C. Similarly, addition of ZnCl$_2$py$_2$ (ref. 41) to a frozen suspension of **4** in benzene afforded (^{tbs}L)Fe$_2$Zn(py) (**6**). Crystals suitable for SC-XRD analysis were obtained from a concentrated solution of **6** in diethyl ether at −33 °C (Scheme 1).

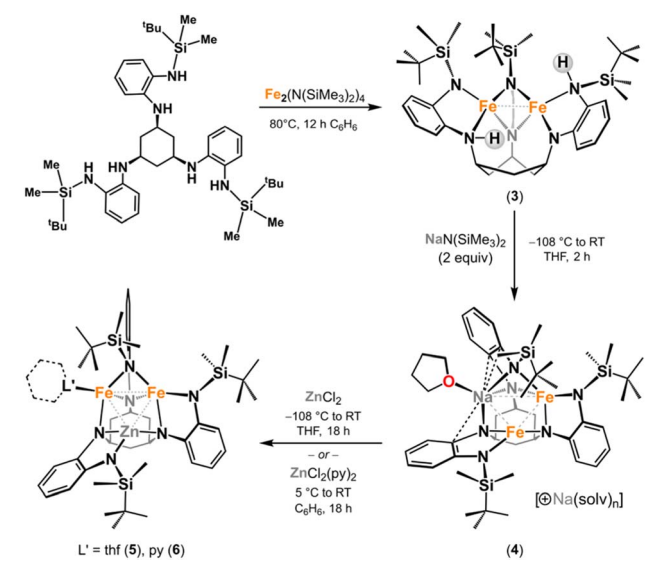

Scheme 1 Synthesis of (^{tbs}L)Fe$_2$Zn(thf) (**5**) and (^{tbs}L)Fe$_2$Zn(py) (**6**).

SC-XRD studies of **5** (Fig. 2a) and **6** (Fig. S37†) reveals C_1-symmetric complexes containing a [Fe$_2$Zn] core, isostructural to **1** and **2**. The average M–M distances of **5** (d_{Fe-Fe}: 2.7354(9) Å, d_{Fe-Zn}: 3.051(1) Å) and **6** (d_{Fe-Fe}: 2.8141(7) Å, d_{Fe-Zn}: 2.9366(8) Å) are longer than the average M–M distances in the tri-iron cores of **1** (2.577(6) Å)[11] and **2** (2.608(1) Å). Stabilization of the triiron core *via* direct exchange pathways results from short Fe–Fe contacts, thus incorporation of zinc, which does not participate in this exchange, increases the average M–M separation.[37] We assigned the two metal sites with the shortest M–M contact as iron, leaving zinc at the three-coordinate site (Fig. 2a). X-ray fluorescence (XRF) spectroscopy was used to determine the bulk metal composition of the crystalline samples. Using a calibration curve to correct for the differential absorption power of the two metals, the Fe : Zn molar ratios were measured as 2.2 : 1 for **5** and 2.1 : 1 for **6**. These values are consistent with the expected 2 : 1 ratio.

Zero-field ^{57}Fe Mössbauer spectroscopy (^{57}Fe MB) analysis of **1** and **2** reveals three iron environments in each (δ, $|\Delta E_Q|$ (mm s^{-1}) (%) for **1**:[36–38] 0.88, *1.29* (28%); 0.37, *1.99* (36%); 0.46, *1.52* (36%); for **2**: 0.33, *1.84* (38%); 0.55, *1.76* (28%); 0.74, *1.39* (33%); Fig. S1†). However, only two quadrupole doublets are observed for **5** and **6**, indicating site-isolated insertion of zinc into the trinuclear core (δ, $|\Delta E_Q|$ (mm s^{-1}) for **5**: 0.60, *1.83* (50%); 0.84, *1.55* (50%); for **6**: 0.61, *1.68* (50%); 0.79, *1.63* (50%); Fig. 2a and S4†). Compared to **1** and **2**, **5** and **6** lack a quadrupole doublet with an isomer shift near 0.3 mm s^{-1}, corresponding to the three-coordinate site in the core.

The electronic structure of **5** was further interrogated by study of its magnetic susceptibility *via* SQUID magnetometry. A plot of X_MT *vs* T indicates that **5** possesses a low-spin ground state (X_MT (2.0 K) = 0.73 cm^3 K mol^{-1}). Beyond 100 K, the susceptibility increases monotonically with temperature, reaching a value of 3.99 cm^3 K mol^{-1} at 300 K (Fig. 3a). Low-temperature magnetization studies of **5** reveal a saturation magnetization value of 0.58 $N_A\mu_B$, suggestive of a diamagnetic ground state for **5** with a small population of paramagnetic states remaining. The electronic structure of **5** stands in contrast to the structurally analogous, maximally high-spin S = 6 triferrous cluster (^{tbs}L)Fe$_3$(thf) (**1**).[21] The susceptibility of **1** increases rapidly from 1.8 to 20 K from an initial value of 13.75 cm^3 K mol^{-1}, reaching a maximum of 19.33 cm^3 K mol^{-1} at 150 K, and diminishing moderately to 17.80 cm^3 K mol^{-1} at 300 K (Fig. 3a). A low-temperature magnetization study of triiron **1** reveals a saturation magnetization value of 8.32 $N_A\mu_B$, which is below the value anticipated for a maximally high-spin S = 6 system, in line with the presence of zero-field splitting (Fig. 3b). The susceptibility and magnetization data of **1** were best fit to a spin-Hamiltonian describing three coupled spins in an equilateral arrangement, providing J = 40(1) cm^{-1}, D = 20.0(9) cm^{-1}, $|E/D|$ = 0.082(7) cm^{-1}, and g = 1.92(1) (see ESI†). These data reveal that in **5**, magnetic coupling of the two iron

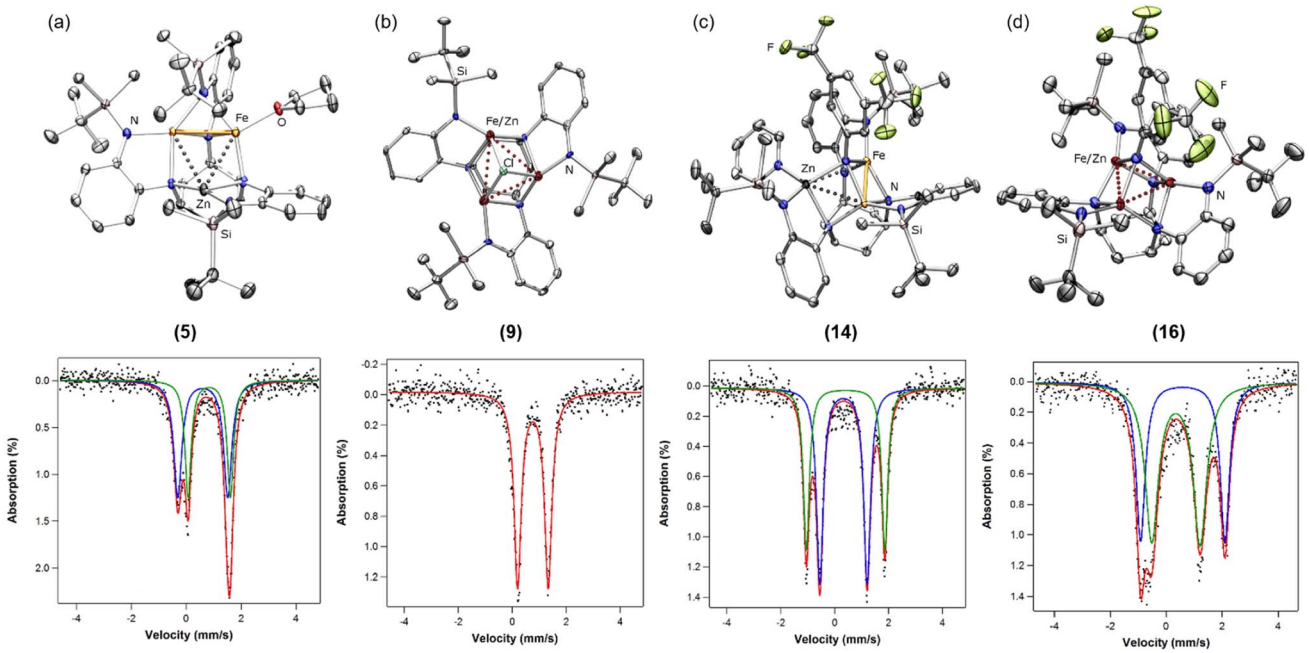

Fig. 2 Solid-state molecular structures and zero-field ^{57}Fe MB spectra of (a) (^{tbs}L)Fe$_2$Zn(thf) (**5**), (b) [NBu$_4$][(^{tbs}L)Fe$_n$Zn$_{3-n}$(μ^3-Cl)] (**9**), (c) (^{tbs}L)Fe$_2$Zn(μ^3-NAr^F)(py) (**14**), (d) [2,2,2-crypt(K)][(^{tbs}L)Fe$_2$Zn(μ^3-NAr^F)] (**16**) with 50% probability ellipsoids. Hydrogen atoms and counter ions omitted for clarity. Zero-field ^{57}Fe MB spectra collected at 90 K. Fitting parameters: δ, $|\Delta E_Q|$ (mm s^{-1}) for (a): 0.60, *1.83* (blue, 50%); 0.84, *1.55* (green, 50%) (b): 0.77, *1.13* (red) (c): 0.33, *1.76* (green, 46%); 0.40, *2.92* (blue, 54%) (d): 0.35, *1.73* (green, 50%); 0.59, *3.01* (blue, 50%).

centers is dominated by antiferromagnetic superexchange through the dianilido bridge, and further suggests that the high-spin ground-state of isostructural (^{tbs}L)Fe$_3$(thf) (**1**) is strongly influenced by the incorporation of a third ferrous ion.

2.2. Redox neutral substrate binding

To test the cluster integrity upon redox neutral substrate binding, tetrabutylammonium chloride was added to a solution of **5** in benzene (Scheme 2). Up to four isostructural products may be formed in this reaction: [NBu$_4$][(^{tbs}L)Fe$_3$(μ^3-Cl)] (**7**), [NBu$_4$][(^{tbs}L)Fe$_2$Zn(μ^3-Cl)], [NBu$_4$][(^{tbs}L)FeZn$_2$(μ^3-Cl)], and [NBu$_4$][(^{tbs}L)Zn$_3$(μ^3-Cl)] (**8**); of these, **7** and **8** were independently synthesized. Crystallization was achieved by diffusion of hexanes into a concentrated solution of the reaction product of **5** and tetrabutylammonium chloride in THF at −33 °C. The XRF spectrum of the crystalline product gave an Fe : Zn ratio of 2.1 : 1 (Fig. S16†). SC-XRD analysis revealed a pseudo C_3-symmetric chloride-bridged cluster (Fig. 2b). Due to the symmetric ligand environment, the metal identity at each site could not be assigned, but the average M–M distance of 2.945(2) Å is longer than in **7** (2.772(1) Å) and shorter than in **8** (2.985(1) Å), consistent with formation of a species containing a mixture of Fe and Zn within the trinuclear core, which we nominally formulate as [NBu$_4$][(^{tbs}L)Fe$_n$Zn$_{3-n}$(μ^3-Cl)] (**9**; $n = 1,2$). The ^{57}Fe MB spectrum of **9** (δ, $|\Delta E_Q|$ (mm s^{-1}): 0.77, *1.13*) is similar to that of **7** (δ, $|\Delta E_Q|$ (mm s^{-1}): 0.72, *1.31*), with spectra of both materials showing just one quadrupole doublet (Table S1† and Fig. 2b). Despite the solid-state structure of **7** revealing three distinct Fe–Fe distances, only one quadrupole doublet in the ^{57}Fe MB spectrum is observed. The similarity of the spectral

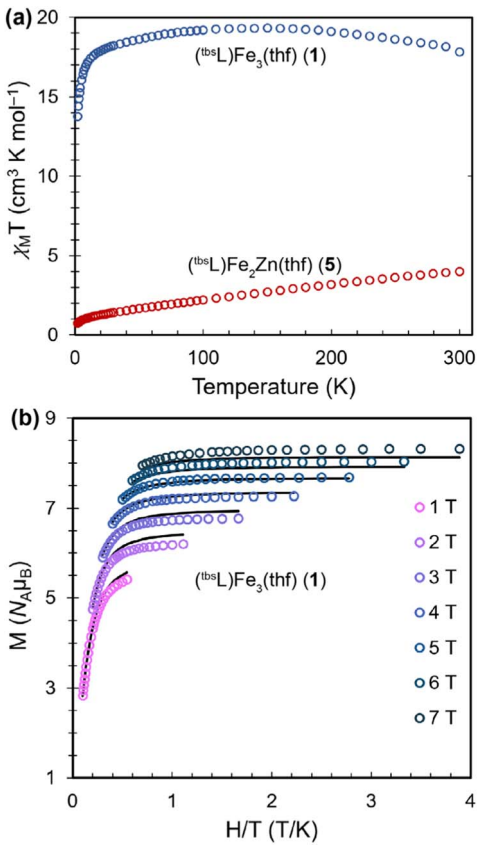

Fig. 3 (a) Plot of χ_MT *vs* *T* for **1** (blue circles) and **5** (red circles). (b) Plot of reduced magnetization for **1** from 1.8–10 K; data are represented as circles, and the fit is represented as black lines.

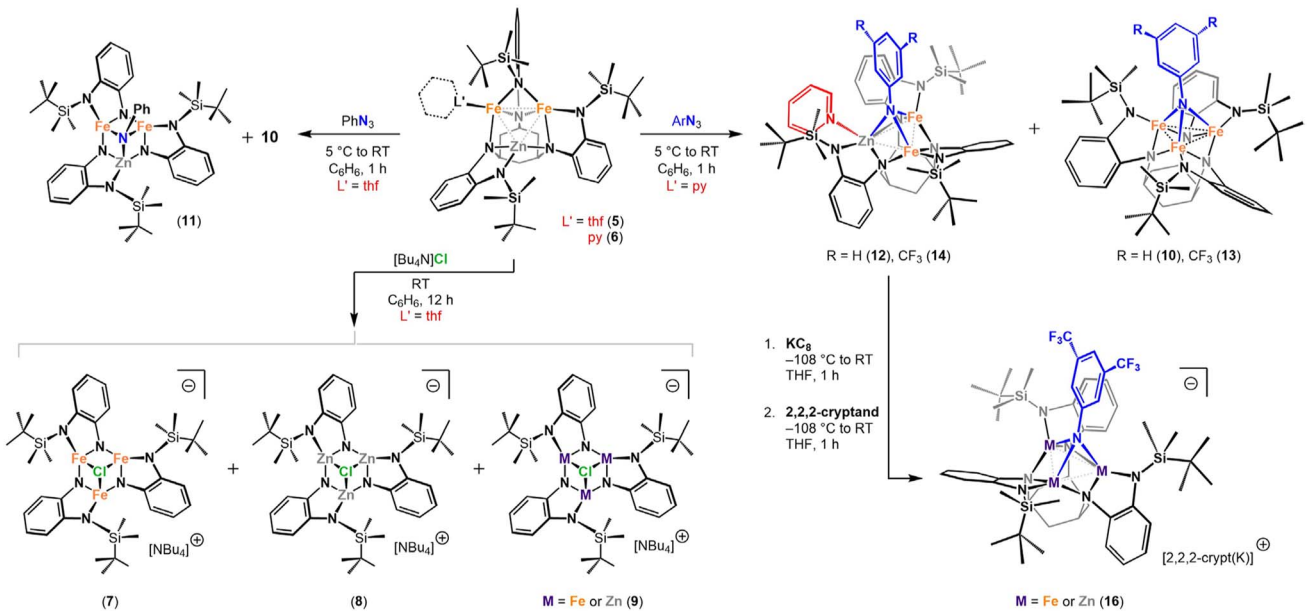

Scheme 2 Reactivity of (^{tbs}L)Fe$_2$Zn(thf) (**5**) and (^{tbs}L)Fe$_2$Zn(py) (**6**).

parameters for **7** and **9** suggest the iron sites are in similar electronic environments, and any Zn in **9** is evenly distributed amongst the three sites, and the diminished symmetry is not adequately resolved by ^{57}Fe MB spectroscopy.

While the bulk metal ratio of (^{tbs}L)Fe$_2$Zn(thf) (**5**) was conserved upon chloride ligation, the ^{1}H NMR spectrum of redissolved crystalline material (Fig. S20†) shows the all-iron and all-zinc clusters [NBu$_4$][(^{tbs}L)Fe$_3$(μ^3-Cl)] (**7**) and [NBu$_4$][(^{tbs}L)Zn$_3$(μ^3-Cl)] (**8**), alongside mixed-metal cluster **9**. These data indicate that chloride anion substitution of THF in **5** results in metal atom redistribution. Indeed, the substitution of a labile ligand for chloride seems to be a determining factor in facilitating metal atom redistribution. Notably, such redistribution reactivity is hindered in an equimolar mixture of the μ^3-halide capped complexes **7** and **8** (Scheme 3). In THF solution, **7** and **8** showed no evidence of metal atom redistribution after 24 h at room temperature, with only trace amounts of mixed-metal products forming after heating to 80 °C, according to ^{1}H NMR spectroscopy (Fig. S21†). In contrast, ^{1}H NMR analysis of a solution containing **5** and tri-ferrous **7** revealed complete consumption of **5** to generate **9**, with some **7** persisting in solution (Scheme 3 and Fig. S22†). In contrast, reaction of **5** with all-zinc **8** produced only trace quantities of **9** at room temperature, with only modestly greater conversion upon heating to 60 °C (Fig. S23†). The qualitatively slower redistribution reactivity of **5** with **8** (compared to **7**) is likely a manifestation of the greater Lewis acidity of the [Zn$_3$] core relative to the [Fe$_3$] core, which results in stronger binding of the μ^3-chloride cap.

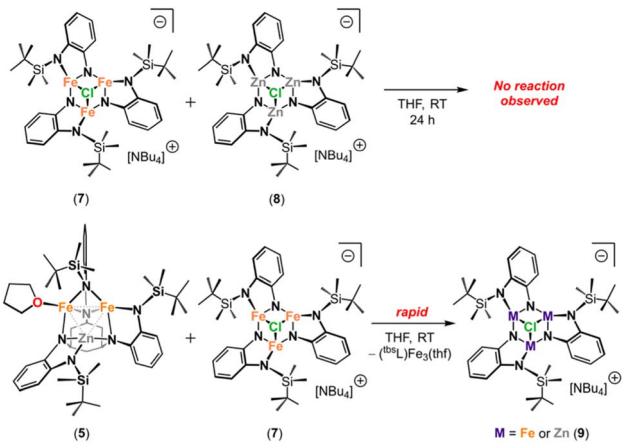

Scheme 3 Metal-atom scrambling screens.

2.3. Reactivity with organic azides

Complexes **5** and **6** were treated with organic azides to probe the lability of the metal sites during oxidative group transfer (Scheme 2). The ^{1}H NMR spectrum of the reaction of **5** with phenyl azide (PhN$_3$) revealed the presence of (^{tbs}L)Fe$_3$(μ^3-NPh) (**10**) as well as a new paramagnetic species, tentatively assigned as (^{tbs}L)Fe$_2$Zn(μ^3-NPh) (**11**). The ^{57}Fe MB spectrum of the crude reaction mixture containing **11** is best fit to a single quadrupole doublet (δ, $|\Delta E_Q|$ (mm s^{-1}): 0.28, *2.31*; Fig. S7†), indicating a major product distinct from **10** (ref. 36) (δ, $|\Delta E_Q|$ (mm s^{-1}): 0.42, *1.97* (67%); 0.42, *1.09* (33%)).

The structure of **11** was confirmed *via* a SC-XRD study. As in **10**, the imido moiety is bound μ^3 to the face of the trinuclear core, and ^{tbs}L is arranged in a C_3-symmetric orientation. An elongation of the average M–M contact in **11** (2.701(1) Å *vs.* 2.530(1) Å in **10**), supports the presence of zinc. Treatment of the py-bound species **6** with PhN$_3$ also resulted in a mixture of a new product and **10** by ^{1}H NMR. Unlike the reaction of **5** with PhN$_3$, crystallization from hexane at −33 °C cleanly separates the new paramagnetic product from **10**.

SC-XRD analysis of this new product reveals a C_1-symmetric cluster, (^{tbs}L)Fe$_2$Zn(μ^3-NPh)(py) (**12**) (Fig. S42†). In contrast to

the reaction of **2** with PhN_3, which produces unsolvated **10**, pyridine remains bound to one metal center in **12**. We assigned the py-bound site as the zinc site as it also features the longest M–M separations (2.7599(6), 3.2059(7) Å). The remaining two atoms are assigned as the iron positions, supported by the short M–M contact between these sites (2.4880(6) Å). The Fe–Fe contact in this species is shorter than all three Fe–Fe contacts in **10**. This shortened Fe–Fe distance is suggestive of an increased M–M interaction, consistent with localization of two-electron oxidation across two iron sites. The ^{57}Fe MB spectrum of **12** exhibits two quadrupole doublets due to the differences in coordination environment at the two iron centers (δ, $|\Delta E_Q|$ (mm s^{-1}): 0.35, *2.76* (49%); 0.33, *1.80* (51%); Fig. S8†). However, the similar isomer shift of the two signals confirms that both iron centers are in the 3+ oxidation state. The XRF spectrum of crystalline **12** gave an Fe : Zn ratio of 2.1 : 1, consistent with a compositionally homogenous [Fe_2Zn] cluster (Fig. S17†).

To quantify metal atom redistribution, **6** was treated with 3,5-bistrifluoromethyl-azidobenzene (3,5-$(CF_3)_2C_6H_3N_3$), which allowed for integration of the product ratio *via* ^{19}F NMR spectroscopy. Two resonances were observed in the ^{19}F NMR spectrum of the reaction mixture in a 7.8 : 1 ratio, where the less intense peak at −69.4 ppm was identified by independent synthesis as the triiron imido (^{tbs}L)$Fe_3(\mu^3$-N(3,5-$(CF_3)_2C_6H_3$)) (**13**), confirming formation of (^{tbs}L)$Fe_2Zn(\mu^3$-N(3,5-$(CF_3)_2$-C_6H_3))(py) (**14**) as the major product. Akin to **12**, cluster **14** can be selectively crystallized and SC-XRD analysis of **14** revealed a structure directly analogous to **12** (Fig. 2c). The XRF spectrum of crystalline **14** yielded an Fe : Zn ratio of 2.1 : 1.

2.4. Outer-sphere electron transfer

The aforementioned experiments demonstrated that metal atom redistribution in open shell clusters can be triggered by ligand substitution and group transfer reactions. We next sought to establish whether outer-sphere electron transfer reactions would elicit the same metal-atom redistribution. To this end, **14** was treated with KC_8 in thawing THF (Scheme 2) and [2.2.2]-cryptand (2,2,2-crypt) was added to sequester the counterion. The ^{1}H and ^{19}F NMR spectra of the reaction mixture contain no signals corresponding to the analogous, independently prepared triiron product [$CoCp^*_2$][(^{tbs}L)$Fe_3(\mu^3$ − NArF)] (**15**) (Fig. S27†). The observation of a single peak in the ^{19}F NMR spectrum suggests the formation of an exclusive imido-bearing cluster; consistently, XRF analysis of this reduction product yielded a Fe/Zn ratio of 1.9 : 1 (Fig. S19†).

Crystals of the product were formed by diffusion of hexanes into a concentrated THF solution at −33 °C. SC-XRD analysis confirmed that the imido ligand remains μ^3-bound, while pyridine has been expelled to form the mixed-metal imido cluster [2,2,2-crypt(K)][(^{tbs}L)$Fe_2Zn(\mu^3$-NAr^F)] (**16**) (Fig. 2d). The three metal sites span a modest range with respect to M–N_{imido} distances from the two molecules in the asymmetric unit (2.010(2)–2.101(3) Å) and M–M separation (2.6660(7)–2.7843(6) Å). Despite its geometric symmetry, **16** exhibits two quadrupole doublets in its ^{57}Fe MB spectrum. While one doublet has a similar isomer shift to that of the two quadrupole doublets in the starting material (0.35 mm s^{-1}), the other increases to 0.59 mm s^{-1} (Fig. 2d), consistent with site-isolated reduction.[42] As it is impossible to discern the metal identity of the three sites by traditional X-ray diffraction, we are currently investigating **16** using resonant X-ray and neutron diffraction to evaluate the metal occupancy at each site.

2.5. Potential mechanisms of metal-atom exchange

We propose the mechanism of metal exchange from the cluster is facilitated by halide addition. While the chloride-capped all-ferrous [NBu_4][(^{tbs}L)$Fe_3(\mu^3$-Cl)] (**7**) and all-zinc [NBu_4][(^{tbs}L)$Zn_3(\mu^3$-Cl)] (**8**) do not undergo metal-atom redistribution upon mixing in solution, we propose that terminal halide coordination to one metal site facilitates exchange. This hypothesis is bolstered by the observed reactivity of (^{tbs}L)Fe_2Zn(thf) (**5**) with either **7** or **8**, which results in variable extents of metal-atom redistribution. Thus, exchange of L′ = thf or py for chloride can lead to ligand reorganization about the mixed metal core to facilitate metal atom excision. Similar reactivity was observed with the related (^{Ph}L)Fe_3 cluster[43] that was found to undergo ligand reorganization to form extended structures, as well as undergo both degenerative iron exchange (as evidenced by isotope exchange) or cobalt for iron exchange upon addition of MCl_2 (M = ^{57}Fe, Co; Scheme 4). The open-shell electronic structure of these complexes makes ligand exchange facile, ultimately favoring formation of products that maximize the stability of the resulting cluster.

Azide binding likely facilitates metal atom extrusion akin to the chloride addition, particularly in instances where the azide ligand is bound in a terminal, μ^1-fashion.[44] While the mixed-metal imido clusters **12** and **14** could be trapped and selectively crystallized, monitoring of the reaction between **6** and ArN_3 indicated metal atom redistribution, as evidenced by the formation of the triiron imido, (^{tbs}L)$Fe_3(\mu^3$-NAr). Again, exchange of L′ for NAr, followed by (^{tbs}L) reorganization about the trinuclear core, can expose the azide-bound metal to facilitate exchange. For example, organic azide binding in the

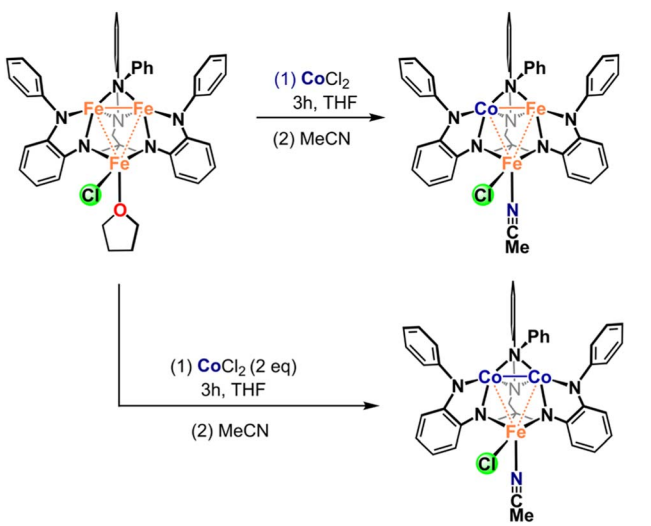

Scheme 4 Metal-atom metathesis from mixed valent cluster (^{Ph}L)Fe_3Cl(thf) see ref. 43.

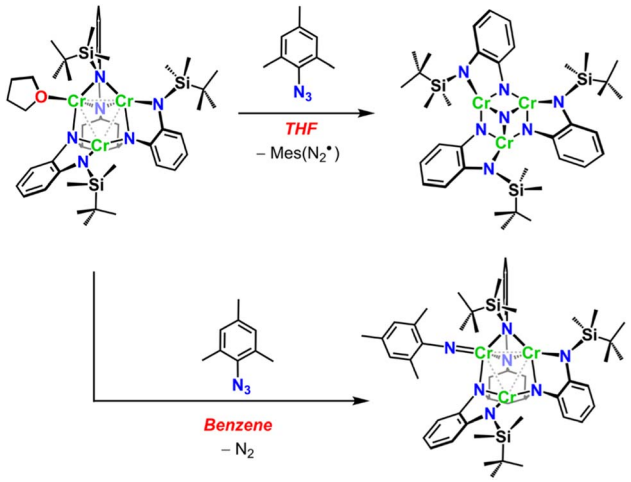

Scheme 5 Solvent directed change in azide breakdown. See ref. 44.

structurally analogous [Cr_3] cluster (^{tbs}L)Cr_3(thf) produces different end products (*i.e.*, bridging nitride *vs.* terminal imido, Scheme 5) depending on how the reacting azide binds to the all-chromous cluster.[44]

We propose that open-faced clusters (*e.g.*, non-symmetrical binding of the templating ligand about the trinuclear core) are necessary to facilitate metal-atom exchange. This is bolstered by the observation that there appears to be little accumulation of free ligand following the metal-atom redistribution. However, we cannot rule out that small amounts of *in situ* generated MX_2 species are aiding in the metal atom redistribution reactions; notably, added MX_2 salts have been shown to catalyze metal-atom exchange in related clusters.[43] Indeed, treatment of **5** with $FeCl_2$ (one equiv.) in THF solution resulted in rapid metal redistribution to form **9** at room temperature (Fig. S24†), although additional unidentified paramagnetic species were also generated, according to ^{1}H NMR spectroscopy. Surprisingly, no redistribution was observed from a mixture of **5** with $ZnCl_2$ (one equiv.) in THF solution, although a diminution of overall resonance intensity in the ^{1}H NMR spectrum (Fig. S25†), as well as a color change from brown to purple, suggested that a transformation had occurred.

3 Conclusions

The foregoing results present the synthesis of [Fe_2Zn] clusters *via* a transmetalation strategy that is more general than our previous transamination strategy for synthesizing bimetallic clusters.[39] We then canvassed the behavior of the [Fe_2Zn] clusters with respect to key reaction types: ligand binding, oxidative group transfer, and outer-sphere electron transfer. Chloride addition to **5** resulted in a mixture of species, where the Fe : Zn of the reaction mixture was maintained, but all-iron **7** and all-zinc **8** were observed in the reaction mixture. Addition of ArN_3 (Ar = Ph; 3,5-$(CF_3)_2C_6H_3$) to **5** or **6** yielded a mixture of two products: the triiron imido product and a mixed-metal imido cluster. In the case of py-bound **6**, the mixed-metal imido included a bound pyridine, allowing for the isolation of [Fe_2Zn] imidos **12** and **14** by selective crystallization. The substitutional homogeneity of **12** and **14** were determined by ^{1}H/^{19}F NMR and ^{57}Fe MB spectroscopies, XRF spectroscopy, and SC-XRD analysis. Finally, outer sphere reduction of py-bound, imido-capped cluster **14** formed reduced mixed-metal imido **16**, with no evidence of metal atom lability from the cluster core.

While metal-atom shuffling was observed upon both neutral substrate-binding and oxidative group transfer chemistry, the integrity of our mixed-metal clusters was maintained upon outer sphere electron transfer when stabilized by an imido capping group. This stabilization is consistent with previous work in cluster chemistry, which has employed bridging ligands to prevent cluster degradation during reactivity.[45–47] The results of this inquiry allow us to demonstrate the dynamic nature of cluster reaction sites. Moreover, knowledge of the factors which confer stability to these clusters can provide valuable information to be used in future catalyst design. Finally, these results illustrate the dynamic nature of bimetallic reaction site substitutions, which may be relevant not only for synthetic cofactor analogues, but also for biological cofactors themselves.

Data availability

Crystallographic data have been deposited at the CCDC under deposition numbers 1993457–1993469. Experimental information and images of experimental data can be found in the ESI.†

Author contributions

C. E. J. and T. A. B. conceived of the hypothesis and experimental designs. C. E. J. performed the experiments, characterization, data collection, and analysis. R. C. H. assisted in synthesis, characterization, and susceptibility measurements. A. K. B., T. M. P., N. X. G., and E. M. provided feedback in data interpretation and carried out several syntheses. N. R., Y. S. C., and S. L. Z. assisted and performed single-crystal X-ray diffraction analysis.

Conflicts of interest

There are no conflicts to declare.

Acknowledgements

This work was supported by grants from the NIH (GM-098395), DOE (DE-SC0019144), and Harvard University. C. E. J. is grateful for an NSF Predoctoral Fellowship. We thank the support to the X-ray core facility from the Major Research Instrumentation (MRI) Program of the National Science Foundation (NSF) under Award Number 2216066. Solid-state structures of **2**, **5**, **6**, **12**, and **16** were obtained at ChemMatCARS Sector 15. NSF's ChemMatCARS Sector 15 is supported by the Divisions of Chemistry (CHE) and Materials Research (DMR), National Science Foundation, under grant number NSF/CHE-1834750. Use of the Advanced Photon Source, an Office of Science User Facility operated for the U.S. Department of Energy (DOE) Office of Science by Argonne National Laboratory, was supported by the U.S. DOE under Contract No. DE-AC02-06CH11357.

Notes and references

1 B. K. Burgess and D. J. Lowe, *Chem. Rev.*, 1996, **96**, 2983–3012.
2 P. C. Dos Santos, R. Y. Igarashi, H. I. Lee, B. M. Hoffman, L. C. Seefeldt and D. R. Dean, *Acc. Chem. Res.*, 2005, **38**, 208–214.
3 B. M. Hoffman, D. R. Dean and L. C. Seefeldt, *Acc. Chem. Res.*, 2009, **42**, 609–619.
4 J. B. Howard and D. C. Rees, *Chem. Rev.*, 1996, **96**, 2965–2982.
5 K. N. Ferreira, T. M. Iverson, K. Maghlaoui, J. Barber and S. Iwata, *Science*, 2004, **303**, 1831–1838.
6 T. J. Wydrzynski, K. Satoh and J. A. Freeman, *Photosystem II The Light Driven Water: Plastoquinone Oxidoreductase*, Springer, Dordrecht, The Netherlands, 2005.
7 J. P. McEvoy and G. W. Brudvig, *Chem. Rev.*, 2006, **106**, 4455–4483.
8 Y. Umena, K. Kawakami, J. R. Shen and N. Kamiya, *Nature*, 2011, **473**, 55–60.
9 N. Cox, D. A. Pantazis, F. Neese and W. Lubitz, *Acc. Chem. Res.*, 2013, **46**, 1588–1596.
10 W. Guo and D. G. Vlachos, *Nat. Commun.*, 2015, **6**, 8619.
11 J. Humphreys, R. Lan and S. Tao, *Adv. Energy Sustainability Res.*, 2021, **2**, 2000043.
12 F. Morales and B. M. Weckhuysen, *Catalysis*, 2006, **19**, 1–40.
13 R. H. Holm, P. Kennepohl and E. I. Solomon, *Chem. Rev.*, 1996, **96**, 2239–2314.
14 A. M. Barrios and S. J. Lippard, *J. Am. Chem. Soc.*, 2000, **122**, 9172–9177.
15 W. Z. Lee and W. B. Tolman, *Inorg. Chem.*, 2002, **41**, 5656–5658.
16 J. S. Kanady, E. Y. Tsui, M. W. Day and T. Agapie, *Science*, 2011, **333**, 733–736.
17 E. Y. Tsui, J. S. Kanady and T. Agapie, *Inorg. Chem.*, 2013, **52**, 13833–13848.
18 S. Zhang, M. M. Melzer, S. N. Sen, N. Celebi-Olcum and T. H. Warren, *Nat. Chem.*, 2016, **8**, 663–669.
19 E. Kim, E. E. Chufan, K. Kamaraj and K. D. Karlin, *Chem. Rev.*, 2004, **104**, 1077–1133.
20 A. J. Jasniewski and L. Que Jr, *Chem. Rev.*, 2018, **118**, 2554–2592.
21 T. M. Powers, A. R. Fout, S. L. Zheng and T. A. Betley, *J. Am. Chem. Soc.*, 2011, **133**, 3336–3338.
22 R. B. Ferreira and L. J. Murray, *Acc. Chem. Res.*, 2019, **52**, 447–455.
23 E. L. Muetterties, *Science*, 1977, **196**, 839–848.
24 O. Einsle and D. C. Rees, *Chem. Rev.*, 2020, **120**, 4969–5004.
25 Y. Hu and M. W. Ribbe, *Coord. Chem. Rev.*, 2011, **255**, 1218–1224.
26 W. Kang, C. C. Lee, A. J. Jasniewski, M. W. Ribbe and Y. Hu, *Science*, 2020, **368**, 1381–1385.
27 M. Can, F. A. Armstrong and S. W. Ragsdale, *Chem. Rev.*, 2014, **114**, 4149–4174.
28 E. C. Wittenborn, S. E. Cohen, M. Merrouch, C. Léger, V. Fourmond, S. Dementin and C. L. Drennan, *J. Biol. Chem.*, 2019, **294**, 13017–13026.
29 E. C. Wittenborn, C. Guendon, M. Merrouch, M. Benvenuti, V. Fourmond, C. Leger, C. L. Drennan and S. Dementin, *ACS Catal.*, 2020, **10**, 7328–7335.
30 E. C. Wittenborn, M. Merrouch, C. Ueda, L. Fradale, C. Leger, V. Fourmond, M. E. Pandelia, S. Dementin and C. L. Drennan, *Elife*, 2018, **7**, e39451.
31 M. Chrysina, E. Heyno, Y. Kutin, M. Reus, H. Nilsson, M. M. Nowaczyk, S. DeBeer, F. Neese, J. Messinger, W. Lubitz and N. Cox, *Proc. Natl. Acad. Sci.*, 2019, **116**, 16841–16846.
32 J. Kern, R. Chatterjee, I. D. Young, F. D. Fuller, L. Lassalle, M. Ibrahim, S. Gul, T. Fransson, A. S. Brewster, R. Alonso-Mori, R. Hussein, M. Zhang, L. Douthit, C. de Lichtenberg, M. H. Cheah, D. Shevela, J. Wersig, I. Seuffert, D. Sokaras, E. Pastor, C. Weninger, T. Kroll, R. G. Sierra, P. Aller, A. Butryn, A. M. Orville, M. Liang, A. Batyuk, J. E. Koglin, S. Carbajo, S. Boutet, N. W. Moriarty, J. M. Holton, H. Dobbek, P. D. Adams, U. Bergmann, N. K. Sauter, A. Zouni, J. Messinger, J. Yano and V. K. Yachandra, *Nature*, 2018, **563**, 421–425.
33 M. Carboni and J.-M. Latour, *Coord. Chem. Rev.*, 2011, **255**, 186–202.
34 E. C. Kisgeropoulos, J. J. Griese, Z. R. Smith, R. M. Branca, C. R. Schneider, M. Högbom and H. S. Shafaat, *J. Am. Chem. Soc.*, 2020, **142**, 5338–5354.
35 E. K. Miller, N. E. Trivelas, P. T. Maugeri, E. J. Blaesi and H. S. Shafaat, *Biochemistry*, 2017, **56**, 3369–3379.
36 T. M. Powers and T. A. Betley, *J. Am. Chem. Soc.*, 2013, **135**, 12289–12296.
37 R. Hernández Sánchez, A. K. Bartholomew, T. M. Powers, G. Ménard and T. A. Betley, *J. Am. Chem. Soc.*, 2016, **138**, 2235–2243.
38 T. M. Powers, A. R. Fout, S. L. Zheng and T. A. Betley, *J. Am. Chem. Soc.*, 2011, **133**, 3336–3338.
39 T. M. Powers, N. X. Gu, A. R. Fout, A. M. Baldwin, R. Hernandez Sanchez, D. M. Alfonso, Y. S. Chen, S. L. Zheng and T. A. Betley, *J. Am. Chem. Soc.*, 2013, **135**, 14448–14458.
40 E. V. Eames, R. Hernández Sánchez and T. A. Betley, *Inorg. Chem.*, 2013, **52**, 5006–5012.
41 J. R. Allan, D. H. Brown, R. H. Nuttall and D. W. A. Sharp, *J. Chem. Soc. A*, 1966, 1031–1034.
42 F. Menil, *J. Phys. Chem. Solids*, 1985, **46**, 763–789.
43 E. V. Eames, R. l. Hernández Sánchez and T. A. Betley, *Inorg. Chem.*, 2013, **52**, 5006–5012.
44 A. K. Bartholomew, C. E. Juda, J. N. Nessralla, B. Lin, S. G. Wang, Y. S. Chen and T. A. Betley, *Angew. Chem., Int. Ed.*, 2019, **58**, 5687–5691.
45 R. C. Ryan and C. U. Pittman, *J. Am. Chem. Soc.*, 1977, **99**, 1986–1988.
46 R. J. Haines, N. D. C. T. Steen and R. B. English, *J. Chem. Soc., Dalton Trans.*, 1984, 515–525.
47 J. A. Cabeza, J. M. Fernandez-Colinas, A. Llamazares, V. Riera, S. Garcia-Granda and J. F. Van der Maelen, *Organometallics*, 1994, **13**, 4352–4359.